



Effect of the Preparation Method of LaSrCoFeO_x Perovskites on the Activity of N₂O Decomposition

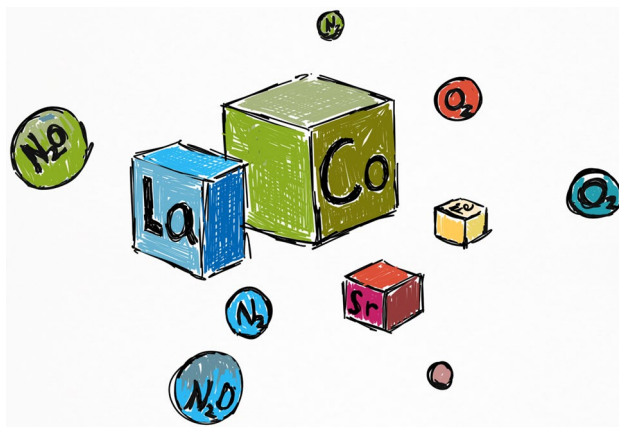
Nia Richards¹ · Luke A. Parker^{1,2} · James H. Carter¹ · Samuel Pattison¹ · David J. Morgan¹ · Nicholas F. Dummer¹ · Stanislaw E. Golunski¹ · Graham J. Hutchings¹

Received: 22 February 2021 / Accepted: 1 April 2021
© The Author(s) 2021

Abstract

N₂O remains a major greenhouse gas and contributor to global warming, therefore developing a catalyst that can decompose N₂O at low temperatures is of global importance. We have investigated the use of LaSrCoFeO_x perovskites for N₂O decomposition and the effect of surface area, A and B site elements, Co–O bond strength, redox capabilities and oxygen mobility have been studied. It was found that by using a citric acid preparation method, perovskites with strong redox capabilities and weak Co–O bonds can be formed at relatively low calcination temperatures (550 °C) resulting in highly active catalysts. The enhanced activity is related to the presence of highly mobile oxygen species. Oxygen recombination on the catalyst surface is understood to be a prominent rate limiting step for N₂O decomposition. Here the reduced strength of Co–O bonds and mobile lattice oxygen species suggest that the surface oxygen species have enhanced mobility, aiding recombination, and subsequent regeneration of the active sites. La_{0.75}Sr_{0.25}Co_{0.81}Fe_{0.19}O_x prepared by citric acid method converted 50% of the N₂O in the feed (T₅₀) at 448 °C.

Graphic Abstract



Keywords Perovskite · Nitrous oxide decomposition · Oxygen vacancies · Mobile lattice oxygen · Surface area · Co–O bond strength

✉ Nia Richards
RichardsN8@cardiff.ac.uk

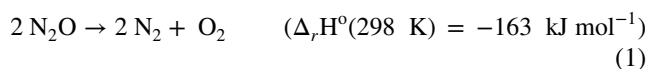
✉ Graham J. Hutchings
Hutch@cardiff.ac.uk

Extended author information available on the last page of the article

1 Introduction

Nitrous oxide (N₂O) has long been considered a potent greenhouse gas and, although only accounting for 332 ppb of the atmosphere, the consequences of uncontrolled emission could be significant with respect to climate change [1].

N_2O has a global warming potential of *ca.* 300 times that of CO_2 , [2, 3] a half-life of double that of CO_2 (114 years compared to an average of 31 years), [4] and an ozone depletion potential comparable to many hydrochlorofluorocarbons (HCFCs). The majority (60%) of global N_2O emissions are generated via anthropogenic sources such as industrial chemical processes including adipic acid production, sewage treatment, the agriculture sector or combustion sources [5, 6]. There are also a number of smaller scale unregulated anthropogenic sources such as hospitals, dental surgeries and veterinary practices where N_2O is used as an anaesthetic and analgesic [7]. Therefore, the development of catalysts that can effectively decompose N_2O (Eq. 1) is of great significance [8].



The importance of finding a suitable catalyst for N_2O decomposition has been known for many years and subsequently there have been various classes of materials that have been used as catalysts, such as ceria-based materials [9, 10], spinels [11, 12] and supported metal nanoparticles [13, 14]. Perovskites are represented by the general formula ABO_3 , where the A site is generally a large rare earth element such as La and the B site typically a smaller transition metal such as Co or Fe. The A site cation is generally catalytically inactive but alters the oxidation state of the B site therefore creating oxygen vacancies [15]. The A sites are typically cations with a charge of 2+/3+, whereas, the B site cations have a charge of 3+/4+. A second A site cation can be incorporated into the structure and the difference in valence state between the cations can lead to further oxygen vacancies or redox couples. Sr or Ce are often used for A site substitution [8]. A perovskite consists of two or more simple oxides that have a high melting point, and the preparation of

a perovskite structure requires high temperature and a long calcination time, which typically leads to high structural and thermal stability [16, 17]. The high temperatures required for the preparation of perovskites typically produce materials with low specific surface areas, usually less than $10 \text{ m}^2 \text{ g}^{-1}$ [16, 18]. However, significant work has been undertaken to produce high surface area perovskite materials [19, 20]. The use of perovskites as solar cells has generated a significant interest in the preparation of these materials [21, 22] and perovskites now show comparable results to that of commercial solar cells [23]. It has been shown previously that oxygen mobility, ease of oxygen vacancy formation, and oxygen storage capacity of a perovskite system can influence the catalytic activity [24, 25]. The oxidation state of the B site cation and the resulting oxygen vacancy can be controlled by substitution of an external cation into the matrix. For example, if a B site cation oxidation state is reduced from B^{4+} to B^{3+} an oxygen vacancy can be formed, due to fewer oxygen atoms being required to balance the charge of the cation. Alternatively, an oxygen vacancy can also be formed by the substitution of an A^{3+} cation with that of an A^{2+} one in the ABO_3 structure. Oxygen vacancies can provide adsorption sites for reactants and subsequent activation can take place, hence their presence in the perovskite structure can be directly linked to their catalytic activity [26].

The most notable perovskite catalysts for N_2O decomposition are presented in Table 1. For example, Russo et al. utilised a solution combustion synthesis method to prepare a LaCoO_3 and reported 100% conversion under conditions of 0.5% N_2O in He at 550 °C, with a T_{50} of 455 °C and an N_2O decomposition rate of $1.3 \text{ mol h}^{-1} \text{ kg}^{-1}$ at 450 °C [27]. Ivanov et al. prepared a series of LaSrMnO_3 catalysts, investigating the effects of the ratio of La and Sr metals in the A site. The optimal La/Sr ratio was found to be $\text{La}_{0.5}\text{Sr}_{0.5}$, resulting in a T_{50} of 750 °C, under conditions

Table 1 Table showing the most relevant perovskites for N_2O decomposition

Perovskite	Conditions	Conversion and T_{50} ^a	N_2O decomposition rate at 450 °C ($\text{mol h}^{-1} \text{ kg}^{-1}$)	Specific surface area ($\text{m}^2 \text{ g}^{-1}$)	Ref.
LaCoO_3	0.5% N_2O WHSV = 120,000 $\text{mL g}^{-1} \text{ h}^{-1}$	T_{50} at 455 °C 100% at 550 °C	1.3	7.7	[27]
$\text{La}_{0.4}\text{Sr}_{0.6}\text{FeO}_3$	0.15% N_2O Contact time $5 \times 10^{-4} \text{ s}$	T_{50} at 815 °C	0* (0.04 at 815 °C)	1	[28]
$\text{Pr}_{0.8}\text{Ba}_{0.2}\text{MnO}_3$	0.5% N_2O , GHSV = 7,500 h^{-1}	T_{50} at 442 °C 100% at 550 °C	1.2	12	[29]
$\text{La}_{0.5}\text{Sr}_{0.5}\text{MnO}_3$	0.15% N_2O GHSV = 30,800 h^{-1}	T_{50} at 750 °C	0* (0.04 at 750 °C)	4.1	[30, 31]
$\text{La}_{0.7}\text{Ba}_{0.3}\text{Mn}_{0.8}\text{In}_{0.2}\text{O}_3$	10% N_2O GHSV = 21,220 h^{-1}	T_{50} at 443 °C 92% at 500 °C	5.9	8	[32]
$\text{Pr}_{0.75}\text{Ba}_{0.25}\text{CoO}_3$	1% N_2O GHSV = 38,000 h^{-1}	T_{50} at 410 °C 100% at 500 °C	32	30	[33]

^aTemperature required to achieve 50% N_2O conversion.

*No activity at 600 °C.

of 0.15% N₂O, and a Gas Hourly Space Velocity (GHSV) of 30,800 h⁻¹ [30, 31]. The group then studied the effect of oxygen mobility on La_{0.4}Sr_{0.6}FeO₃, by doping LaSrFeO₄ ferrite into the structure. The La_{0.4}Sr_{0.6}FeO₃ doped with ca. 10 wt% LaSrFeO₄ was the most active catalyst, with a T₅₀ of 815 °C under the same conditions. The improvement in activity was attributed to the increased mobility of lattice oxygen, highlighting how this is a key factor for N₂O decomposition [28].

Takita et al. probed the effect of varying A and B site metal ratios on N₂O decomposition using a LaBaMnInO₃ catalyst. The most active catalyst was considered to be La_{0.7}Ba_{0.3}Mn_{0.8}In_{0.2}O₃, converting 92% N₂O at 500 °C (T₅₀ 443 °C and N₂O decomposition rate of 5.9 mol h⁻¹ kg⁻¹ at 450 °C) under conditions of 10% N₂O in He at 20 mL min⁻¹ [32]. Kumar et al. reported that it is possible to achieve a similar T₅₀ using a Pr_{0.8}Ba_{0.2}MnO₃ catalyst prepared by impregnation. Pr_{0.8}Ba_{0.2}MnO₃ catalyst was able to achieve 100% N₂O conversion at 550 °C (N₂O decomposition rate of 1.2 mol h⁻¹ kg⁻¹ at 450 °C) under conditions of 0.5% N₂O, balance He and a GHSV of 7500 h⁻¹ [29]. The high activity of the catalysts prepared by Kumar et al. was associated to the enhanced redox properties due to the ratio of Mn^{4+/3+} and the resulting charge compensation effect due to the substitution of Ba into the A site. Previously we have shown it is possible to achieve a T₅₀ of 410 °C (N₂O decomposition rate of 32 mol h⁻¹ kg⁻¹ at 450 °C) using a Pr_{0.75}Ba_{0.25}CoO₃ catalyst, prepared by supercritical anti-solvent precipitation [33]. The catalysts prepared by Kumar et al. and Hutchings and co-workers are amongst the most active perovskites for N₂O decomposition reported in the literature to date.

In this work we investigate the controlling factors for preparing a perovskite catalyst for N₂O decomposition. Surface area, redox capabilities, oxygen mobility, A and B site elements, and Co–O bond strength are all investigated. The rate-limiting step in the decomposition of N₂O is typically the recombination of oxygen on the active site [34–40], if the proximity of the atomic oxygen species is greater than the interaxial distance of oxygen then the bond is unlikely to form and be desorbed as molecular oxygen, therefore blocking an active site [41, 42]. However, if the Co–O bond is weak, the mobility of the oxygen can be improved as it is more able to move around the surface of the catalyst and can recombine with surface oxygen, regenerating the active site. Therefore, producing a catalyst with a relatively weak Co–O bond is advantageous. Here, we have shown that this is the case in the most active catalysts by use of H₂-TPR. H₂-TPR and O₂-TPD have been used to confirm the presence of redox properties, including highly mobile oxygen species. The resulting low T₅₀ of 448 °C (N₂O decomposition rate 22.8 mol h⁻¹ kg⁻¹ at 450 °C), highlights the need for careful catalyst design to maximise the decomposition rate.

2 Experimental

2.1 Catalyst Preparation

2.1.1 Citric Acid Preparation Method

Benchmark perovskite based catalysts were prepared by citric acid preparation as described by Fierro et al. [43]. Metal nitrates were dissolved in deionised water (50 mL) while stirring at 50 °C in a round bottom flask. Citric acid (Sigma Aldrich, > 99.95%) (metal: citric acid = 1:2 molar ratio) was added to the solution and the temperature increased to 90 °C. After 30 min the temperature was increased to 110 °C and stirred for 16 h to give a dry powder. Following grinding, all catalysts were pre-treated in an oven at > 200 °C (details given in Table 3) with a ramp rate of 1 °C min⁻¹ to ensure citric acid combustion, as indicated by TGA. These materials were calcined in flowing air at a suitable temperature, for 3 h at 1 °C min⁻¹ to form a pure phase perovskite, as determined by in situ X-ray diffraction (XRD).

2.1.2 Oxalic Acid Preparation Method

Perovskite catalysts with enhanced phase purity were prepared using oxalic acid as a precipitation agent, based on the work by Fan et al. [44]. Metal nitrates were added in the appropriate ratios totalling 0.02 mol of metal to ethanol (200 mL, Sigma Aldrich, 99.8%) and stirred. Once the metal salts were dissolved, oxalic acid (0.024 mol, Sigma Aldrich, > 99%) was added and the solution was aged for 2 h at room temperature. After aging, the solution was filtered and washed with ethanol (500 mL) and dried (110 °C, 16 h). The resulting solid was pre-treated at 300 °C, followed by calcination in flowing air at a suitable temperature to form a pure phase perovskite, as determined by in situ XRD.

2.1.3 Supercritical Anti-Solvent (SAS) Preparation Method

Perovskite catalysts were prepared using the supercritical anti-solvent (SAS) precipitation method is based on a method previously reported [45–48]. A mixture of metal acetylacetonate hydrate and acetate precursor salts were dissolved in ethanol (Sigma Aldrich 99.8%) together with 5% deionised water. SAS experiments were performed using apparatus manufactured by Separex. CO₂ (99.99%, BOC) was pumped through the system (held at 150 bar, 40 °C) via the outer part of a co-axial nozzle at a rate of 12 kg h⁻¹ (41 Hz). The metal salt solution was concurrently pumped through the inner nozzle using an Agilent HPLC pump at a rate of 4 mL min⁻¹. At this point, the solvent rapidly solubilises into the surrounding supercritical CO₂, causing

the precipitation of the metal precursors. This was recovered on a stainless-steel frit, while the CO₂-solvent mixture passed downstream, where the pressure was decreased to separate the solvent and CO₂. Precipitation was carried out for 120 min followed by a purge of the system with CO₂ for 1 h under 150 bar and 40 °C. The system was then depressurised, and the dry powder collected. The resulting SAS precipitates were then pre-treated at 300 °C, followed by calcination in flowing air at a suitable temperature to form a pure phase perovskite, as determined by in situ XRD.

2.2 N₂O decomposition

All reactions were performed at atmospheric pressure in a continuous-flow fixed-bed reactor. A reactor tube (4.6 mm internal diameter, stainless steel) was packed with catalyst (0.0625 g) between two layers of quartz wool. Reactions were performed over the temperature range of 200–600 °C, with a flow rate of 100 mL min⁻¹ (GHSV: in the range of 35,000 to 40,000 h⁻¹). The gas feed was composed of 1% N₂O/He. All outgoing gaseous products were analysed online using an Agilent 7890B Gas Chromatograph (GC) (columns: Hayesep Q (80–100 mesh, 1.8 m) MolSieve 5A (80–100 mesh, 2 m) fitted with a thermal conductivity detector.

The N₂O decomposition rate at a given temperature (mol_{N₂O} h⁻¹ kg_{cat}⁻¹ shortened to mol h⁻¹ kg⁻¹) is given by the equation:

$$\frac{\text{Conversion at given temperature(\%)} \times \text{Flow rate of N}_2\text{O}(\text{mol h}^{-1})}{\text{Catalyst weight}(\text{kg})}$$

2.3 Catalyst characterisation

X-ray photoelectron spectroscopy (XPS) was performed on a Thermo Fisher Scientific K-alpha⁺ spectrometer. Samples were analysed using a micro-focused monochromatic Al X-ray source (72 W) over an area of approximately 400 microns. Data was recorded at pass energies of 150 eV for survey scans and 40 eV for high resolution scan with 1 eV and 0.1 eV step sizes respectively. Charge neutralisation of the sample was achieved using a combination of both low energy electrons and argon ions. Data analysis was performed in CasaXPS using a Shirley type background and Scofield cross sections, with an energy dependence of -0.6 eV.

Powder X-ray Diffraction (XRD) analysis was performed on a PANalytical X'Pert Pro diffractometer using a Ni-filtered CuKα radiation source operating at 40 kV and 40 mA. Standard analysis was performed using a 40 min run with a back filled sample holder. Patterns were identified using the International Centre for Diffraction Data Powder

Diffraction File. Perovskite phase purity was determined using the International Centre for Diffraction Database (ICDD). Phases were assigned using the 'search and match' function in X'Pert Highscore software. Phase identification is performed by comparing the X-Ray diffraction pattern with known reference data in the ICDD. When two or more phases are present it is possible to achieve a percentage of each, the software uses the information the powder diffraction file (PDF) associated to produce the values, this is semi-quantitative and the technique that has been used in this manuscript. It was assumed that no amorphous regions were present due to the high calcination temperatures used.

In situ XRD was performed using a PANalytical X'Pert Pro diffractometer using a Ni-filtered CuKα radiation source operating at 40 kV and 40 mA, fitted with a cell that allows temperature control and gas flow using Bronkhorst mass flow controllers. Characterisation was controlled via software, the 'Data collector' program was used to set temperature, run time and repeats measurements. Patterns were identified using the International Centre for Diffraction Data Powder Diffraction File.

Thermogravimetric Analysis (TGA) was performed using a Perkin Elmer TGA 4000, with 10 mg sample with 50 mL min⁻¹ air and a ramp rate of 5 °C min⁻¹, from 30 to 800 °C. Mass losses were recorded as changes in mg and converted into a percentage of the total mass of the sample. The metal precursors along with precipitating agents used in this study were analysed to determine their decomposition temperatures, the mass loss profiles are shown in Fig. S1a–j. Due to the ramp rate of 5 °C min⁻¹ there is likely to be a delay of ±20 °C to the final decomposition event when compared to a calcination that is held at a temperature. The secondary profile given with dashed lines in the TGA profile are the derivative of temperature.

Oxygen Temperature Programmed Desorption (O₂-TPD) profiles were performed using a ChemBET TPR/TPD equipped with a TCD to monitor oxygen evolution. A pre-treatment in He up to 550 °C was performed, followed by doping of oxygen using 10% O₂/He at 550 °C, the sample was cooled to room temperature and the gas changed to He, followed by desorption of oxygen up to 850 °C at 10 °C min⁻¹ and held for 10 min at T_{max}, using an attenuation of 2, TCD sensitivity of 150 and flow 30 mL min⁻¹. The sample mass was typically 60 mg.

Nitrogen adsorption isotherms were collected using a Quantachrome Quadrasorb evo. A 20-point analysis was performed using N₂ as the adsorbate gas. Samples were degassed for 14 h at 300 °C prior to analysis. Analysis was carried out at -196 °C with P₀ measured continuously. Free space was measured post analysis with He. The data was analysed using the BET method.

TPR was performed using a ChemBET TPR/TPD equipped with a TCD to monitor hydrogen uptake. A

pre-treatment in He up to 150 °C was performed, followed by a reduction in 10% H₂/Ar up to 800 °C, held for 30 min at T_{max}, using an attenuation of 4, TCD sensitivity of 150 and flow 15 mL min⁻¹. The sample mass used was typically between 40 and 50 mg.

MP-AES was carried out using an Agilent 4100 MP-AES utilising Agilent MP expert software. Calibration samples were prepared by dilution of a standard metal solution with deionised water. A minimum of 4 calibration plots were used per analysis. Solid catalyst samples (50 mg) were dissolved in aqua regia (4 mL diluted to 50 mL with deionised water) to give a pre-calculated approximate metal concentration.

3 Results and Discussion

Initially, two Sr_xCo_yM_z-based perovskite materials (where M = La or Fe) were prepared by a sol-gel method with citric acid, as previously reported [43, 49–55]. La_{0.75}Sr_{0.25}CoO_x (denoted LSC) and SrCo_{0.81}Fe_{0.19}O_x (denoted SCF) were prepared by the combination of citric acid and metal nitrates using a molar ratio of 2:1. Citric acid combustion occurs between 150 and 200 °C, as highlighted in the thermal analysis of LSC (Fig. 1a), with a rapid weight loss at 170 °C. This is also accompanied by the decomposition of La nitrate, followed by further weight losses at 300 °C due to La and Co nitrate decomposition with a final decomposition event seen at 600 °C due to the decomposition of Sr nitrate. To form a pure phase perovskite, the catalyst precursor was treated at an appropriate temperature, as determined by in situ XRD. When performing in situ XRD, the sample must be packed into a sample holder; it is crucial that when the sample is heated, the sample remains flat and the holder fully packed to ensure that the incidence angle of the X-rays remain consistent. Therefore, the catalyst must be pre-treated to limit

mass loss when obtaining in situ XRD patterns. For this catalyst, 400 °C was chosen as the precursor has mostly decomposed below this point; 70% of the catalyst mass had been lost (Fig. 1a).

From the in situ XRD of LSC given in Fig. 1b it is possible to see the growth of the principal perovskite phase via the reflection at 34° 2θ as the temperature increases from 550 to 850 °C. At 850 °C the perovskite phase was 98% pure, with a reflection seen due to the presence of CoO. This temperature was selected as a suitable calcination temperature, due to the extended length of time the sample was held at the maximum temperature, consequently the purity should increase. This temperature was also deemed suitable from the TGA profile (Fig. 1a) as all major decomposition events had occurred prior to this.

The TGA profile of SCF is given in Fig. 2a, where two decomposition events below 350 °C were noted and ascribed to the decomposition of Co and Fe nitrates, and the citrate precursor. The final mass loss was due to the decomposition of Sr nitrate. 550 °C was determined as a suitable pre-treatment temperature prior to performing in situ XRD analysis. The in situ XRD of SCF given in Fig. 2b illustrates the profile changes over the temperature range of 550 to 850 °C. Here, small differences can be observed as the temperature increases from 550 to 800 °C with a reduction of the reflections present at 24, 26 and 36.5°. This is paired with the formation of new reflections, most notably at 32 and 27°, that are present in the final material at 850 °C. A pure phase SCF perovskite is not formed at 850 °C as a Co₃O₄ impurity is formed during the heat treatment. Therefore, a higher calcination temperature of 900 °C was required (the maximum operating temperature of the furnaces), resulting in a perovskite phase purity of 81%.

XRD of the final calcined perovskite structures of LSC and SCF are shown in Fig. S2. SCF contains three reflections

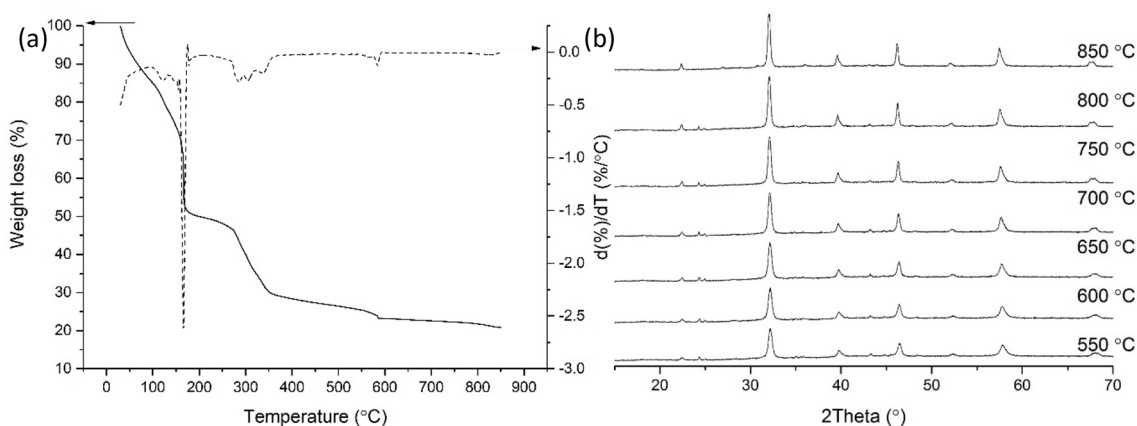


Fig. 1 **a** TGA of LSC up to 850 °C at 5 °C min⁻¹ in air at 50 mL min⁻¹. The secondary profile given with dashed lines in the TGA profile are the derivative of temperature. **b** In situ XRD of LSC treated to 400 °C prior to analysis heated from 550 to 850 °C in air (25 mL min⁻¹)

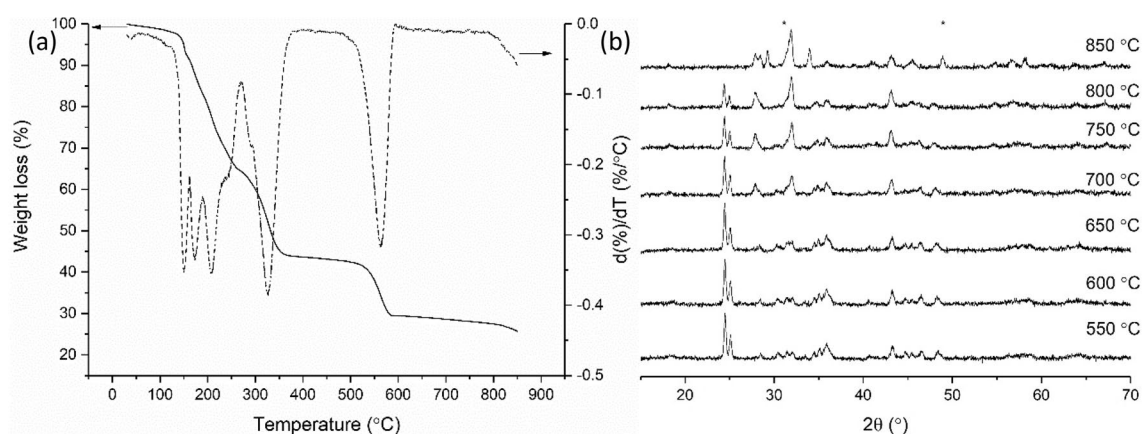


Fig. 2 **a** TGA of SCF up to 850 °C at 5 °C min⁻¹ in air at 50 mL min⁻¹. The secondary profile given with dashed lines in the TGA profile are the derivative of temperature. **b** In situ XRD of SCF

treated to 400 °C prior to analysis heated from 550 to 850 °C in air (25 mL min⁻¹). *Marks Co₃O₄ impurity

at 18.5, 36.8 and 65.6° (2θ) due to the presence of a Co₃O₄ impurity, whereas LSC contains one reflection at 36.7° (2θ) due to the presence of a CoO impurity. All other reflections are due to the perovskite structure.

Analysis of the O 1s region in XPS gives an indication of the species of oxygen present on the surface of the catalyst. There are four notable oxygen species typically observed for perovskite oxides: lattice oxygen (O²⁻) from lanthanide elements (528.6 eV) [56–59], lattice oxygen species due to Co/Fe (ca. 529.5 eV) [60–63], surface hydroxyl species (OH⁻) at 531.0 eV [64], and a species at 533.0 eV, typically ascribed to water [65–67]. The water is trapped within the lattice, rather than being physisorbed on the surface as this would be removed under the ultra-high vacuum conditions required for XPS, unless the surface is hygroscopic, some adsorbed water can remain. Lattice oxygen is also referred

to as β-oxygen, and oxygen vacancies are referred to as α-oxygen [26, 68].

The O 1s region of the spectra of LSC (Fig. 3) shows all four species of oxygen present. Most notably the lanthanide lattice oxygen species made up a large proportion, ca. 42% of the O 1s region. The rest were lattice oxygen from transition metal species and hydroxyl species (breakdown provided in Table S2). Conversely, for the SCF catalyst this is drastically different; lattice oxygen makes up just 1% of the observed oxygen species (Fig. 3). The surface does not contain these lattice oxygen species, instead the carbon region indicates that the surface contains a thin layer of carbonate species that could have formed when Sr came into contact with the atmosphere [69, 70]. There is a large peak at 531 eV in the O 1s spectra that can either be a contribution from hydroxyl OH⁻ or carbonate CO₃²⁻ species. To determine

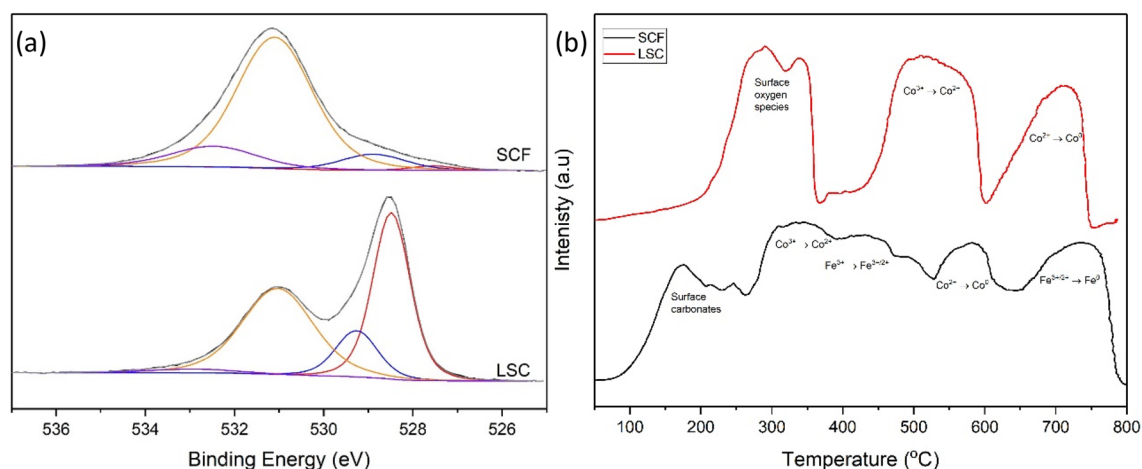


Fig. 3 **a** XPS O 1s region of LSC and SCF catalysts. Fittings: red—lattice O²⁻, blue—lattice O²⁻-transition metal, orange—hydroxyl species OH⁻ or CO₃²⁻ (majority CO₃²⁻ in SCF), and purple—molecular

water on surface. **b** H₂-TPR of LSC and SCF catalysts, performed at 5 °C min⁻¹ up to 800 °C, under a flow of 10% H₂/Ar

which species is present, the carbon region must be studied. If a peak is present at 289.4 eV this is due to the presence of carbonate. In the case of SCF the contribution is from a carbonate species, as confirmed by the carbon spectra shown in Fig. S3 [71]. The LSC perovskite has a small insignificant peak in the carbon region indicating that the oxygen species present is mainly OH⁻. The lanthanum 3d XPS spectra (Fig. S4) shows that all lanthanum containing catalysts have both lanthanum oxide and lanthanum carbonate present. This explains why the LSC catalyst has a small peak at 289.4 eV, without having a large contribution from strontium carbonate. This is further confirmed by the comparison of the C 1s peak at 289 eV and O 1s peak at 531 eV discussed later in the manuscript. The Sr carbonate species is hygroscopic, as indicated by the large peak assigned to molecular water on the surface at 533 eV, *ca.* 14% of the O 1s spectra. Notably, the oxide of Sr is found at a slightly lower binding energy than other elements, with a response seen at 527 eV [72, 73]. The lack of lattice oxygen observed may be a result of the surface sensitive nature of XPS with an analysis depth of *ca.* 8–10 nm. Therefore, an abundance of lattice oxygen in the bulk will not be represented. Additionally, the presence of the carbonate on the surface would limit the ability to detect the lattice oxygen in the bulk. The presence of the carbonate is expected to limit the catalytic activity of the perovskite.

The H₂-TPR profile can indicate the reducibility of the perovskites, where the reducibility is linked to its ability to release oxygen from the perovskite structure by reacting with H₂. H₂-TPR also gives an indication to the strength of the Co–O bond: the weaker the bond the more mobile the oxygen species, and the lower the Co reduction temperature [74]. The reduction of surface-adsorbed O species or non-stoichiometric excess oxygen reduction of oxygen species, this can include oxygen adsorbed on the oxygen deficiency, take place between 200 and 300 °C [75, 76]. This is followed by the step-wise reduction of Co³⁺ to Co²⁺ between 200 and 360 °C and Co²⁺ to Co⁰ between 450 and 540 °C [77, 78]. Fe is the only other reducible metal in these catalysts, both La and Sr are not reducible under the conditions studied [79, 80]. Fe reduction takes place in the following steps: Fe³⁺ to Fe^{3+/2+} at *ca.* 300 °C, followed by the reduction of Fe^{3+/2+} to Fe⁰ at around 700 °C [81]. The H₂-TPR of LSC and SCF are shown in Fig. 3b, SCF shows the initial reduction of surface oxygen species and carbonates (< 250 °C), followed by the simultaneous reduction of Co³⁺ to Co²⁺ and Fe³⁺ to Fe^{3+/2+} between 300 and 500 °C, followed by the reduction of Co²⁺ to Co⁰ between 500 and 600 °C, with the final step due to the reduction of Fe^{3+/2+} to Fe⁰ between 650 and 790 °C. The H₂-TPR of LSC is more difficult to interpret as the reduction temperatures are far higher than expected. The reduction of surface oxygen species takes place between 200 and 350 °C followed by the reduction of Co³⁺ to Co²⁺ between 450 and 600 °C, followed by the final reduction of Co²⁺ to

Co⁰ between 600 and 750 °C. As the reduction of Co in LSC and SCF takes place at the expected temperatures the Co–O bond strength would be anticipated to be intermediate.

Table 2 contains the surface area data for the LSC and SCF, with LSC having the highest (15 m² g⁻¹). This is likely a result of a lower calcination temperature, as higher calcination temperatures can lead to lower surface areas [16, 17, 43, 82, 83]. This is apparent with the SCF catalyst, which was calcined at 900 °C, and has a surface area of 7 m² g⁻¹, however the perovskite is not 100% pure, a Co₃O₄ phase is also present that can have different textural properties. The temperature required for 50% conversion of N₂O (T₅₀) over the LSC catalyst is 468 °C, compared to 585 °C over the SCF catalyst (Fig. 4). The lower activity of the SCF catalyst indicates that lattice oxygen species are crucial for the decomposition of N₂O (Fig. 4). This is due to N₂O adsorption taking place at a vacant site, such as a coordinatively unsaturated metal, followed by decomposition and release of N₂, with adsorbed O. The rate-limiting step of this reaction is the recombination of oxygen [34, 35], therefore, a high lattice oxygen concentration with sufficient mobility can aid this reaction step and produce a more active catalyst. In the case of SCF, the phase impurities present have a negative impact on the activity, with temperatures greater than 600 °C required for significant conversion.

3.1 Citric Acid Preparation of La_{0.75}Sr_{0.25}Co_{0.81}Fe_{0.19}O_x (LSCF Citric)

Based on the reaction data shown in Fig. 4 and catalyst characterisation data from Table 2, it is apparent that higher surface area, phase purity and lattice oxygen concentration lead to a more active catalyst. Therefore, the two perovskite metal ratios were combined with the idea that introducing secondary metals into both the A and B site would facilitate redox coupling and allow for a lower calcination temperature to form a pure phase perovskite resulting in a higher surface area and subsequently an increase in activity.

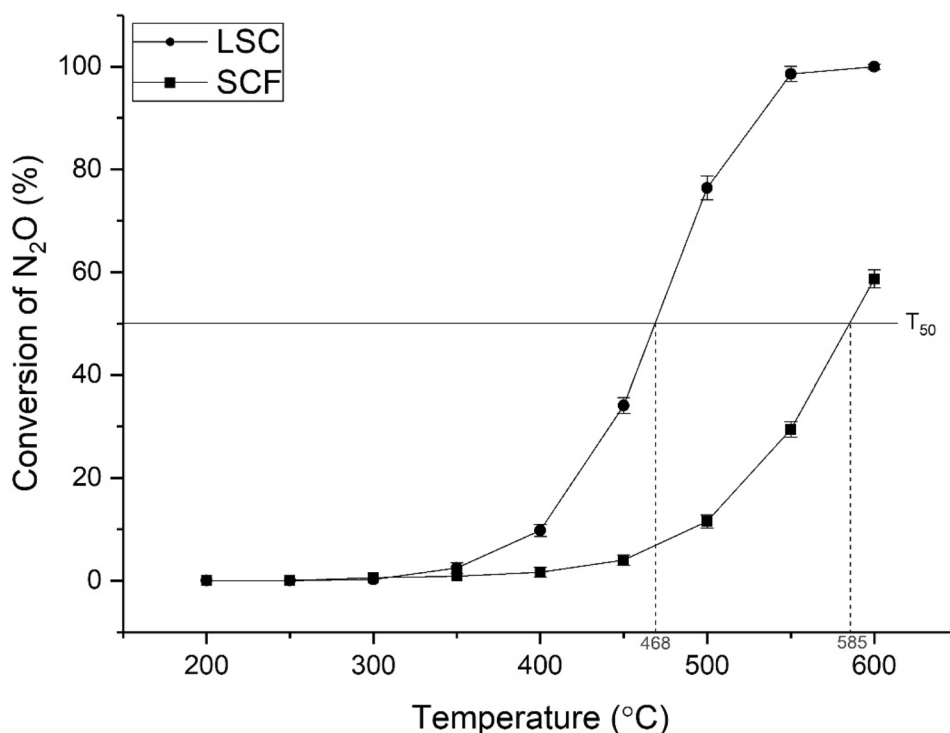
Table 2 Calcination temperature, specific surface area, phase purity, lattice oxygen percentage and the temperature required for 50% conversion (T₅₀)

Catalyst	Perovskite phase purity (%) ^a	Calcination temperature (°C)	Specific surface area (m ² g ⁻¹)	T ₅₀ (°C)	Surface lattice O (%) ^b
LSC	98	850	15	468	42
SCF	81	900	7	585	1

^aPerovskite phase purity calculated using XRD diffraction pattern and the ratio between the single perovskite phase and any impurities.

^bLattice oxygen calculated by the ratio of lattice oxygen species to the sum of molecular water, transition metal lattice oxygen, hydroxyl species, as derived from XPS measurements.

Fig. 4 Graph showing N_2O decomposition using perovskite-based catalysts. Reaction Conditions: 1% N_2O/He , total flow 100 mL min^{-1} . Legend: filled square—SCF, filled circle—LSC. If error bars are not present, then smaller than symbol and less than 1%



A $La_{0.75}Sr_{0.25}Co_{0.81}Fe_{0.19}O_x$ perovskite was prepared by the citric acid precipitation method and henceforth referred to as LSCF citric.

Optimisation of the perovskite final calcination temperature was performed using TGA and in situ XRD as detailed previously, the details are provided in the SI. A final calcination temperature of $550\text{ }^\circ\text{C}$ was deemed appropriate.

Previous reports suggest that a high surface area perovskite will lead to an active N_2O decomposition catalyst [8, 15, 84]. The specific surface area of the LSCF citric perovskite was measured at $13\text{ m}^2\text{ g}^{-1}$ which is comparable to the LSC citric material ($15\text{ m}^2\text{ g}^{-1}$). Most attempts at increasing the surface area of perovskites have found success through supporting perovskites on high surface area supports. Alini et al. supported a $CaMn_{0.6}Cu_{0.4}O_3$ perovskite on a CeO_2-ZrO_2 support [84]. The surface area of this catalyst increased from 15 to $63\text{ m}^2\text{ g}^{-1}$, with a 10% perovskite loading, the increase in surface area was due to the presence of the CeO_2-ZrO_2 support that the perovskite was dispersed on. The N_2O conversion over the catalyst increased from 58 to 67% at $500\text{ }^\circ\text{C}$. The authors linked both the increase in surface area and the contribution of the support's oxygen mobility to the increase in observed activity [84]. However, Dacquin et al. reported that it was possible to increase the surface area of a $LaCoO_3$ from 12 to $50\text{ m}^2\text{ g}^{-1}$ by changing the preparation method from templating to reactive grinding. [85] It was stated that the highest surface area catalysts were the most active for N_2O decomposition despite the phases of the perovskite present remaining constant between preparation

methods. Therefore the increase in activity was ascribed to the increases in specific surface area and the higher density of oxygen vacancies present [85].

3.2 Supercritical Anti-Solvent Precipitation: $La_{0.75}Sr_{0.25}Co_{0.81}Fe_{0.19}O_x$ (LSCF SAS)

Previously, we have shown that the surface area of a perovskite can be significantly increased via a (SAS) preparation method [33]. A $La_{0.75}Sr_{0.25}Co_{0.81}Fe_{0.19}O_x$ (LSCF SAS) perovskite was prepared by SAS, the appropriate calcination temperature was determined by TGA and in situ XRD as $800\text{ }^\circ\text{C}$, further details are provided in the SI. As such a high temperature is required for calcination ($800\text{ }^\circ\text{C}$), which resulted in a specific surface area of $12\text{ m}^2\text{ g}^{-1}$. An XRD measurement was performed at room temperature after calcination at $800\text{ }^\circ\text{C}$ and confirmed a single rhombohedral phase present.

3.3 Oxalic Acid Precipitation Method $La_{0.75}Sr_{0.25}Co_{0.81}Fe_{0.19}O_x$ (LSCF Oxalic)

To further investigate the effect of surface area, purity and lattice oxygen concentration on the activity of perovskite catalysts for N_2O decomposition, the LSCF perovskite was prepared using an oxalic acid-based method. Oxalic acid facilitates the formation of a metal oxalate network, which then collapses to form a well dispersed metal oxide [33, 44, 86, 87]. In situ XRD and TGA were used to determine a

suitable calcination temperature of 750 °C, further details are provided in the SI. An XRD measurement was performed after calcination and confirmed a single-phase present, confirming the rhombohedral structure. The final structure of all LSCF perovskites are shown in Fig. S7, LSCF is not restricted to one structure, as both a rhombohedral and cubic structure are noted. The specific surface area of the LSCF oxalic sample was calculated to be 14 m² g⁻¹ following nitrogen adsorption experiments.

4 Discussion

The LSCF perovskite samples were used as catalysts for the decomposition of N₂O and compared to the activity of the ternary perovskite materials as illustrated in Fig. 4. LSCF citric demonstrated higher activity than both the original LSC and SCF catalysts, with a T₅₀ of 448 °C (Table 3), this is a decrease from 468 °C (LSC) and 585 °C (SCF). The incorporation of Fe into the B site of the LSC catalyst allowed the use of a lower calcination temperature to form a phase pure perovskite. The surface area of the catalyst remained consistent at 15 m² g⁻¹ without Fe (LSC), to 13 m² g⁻¹ with Fe. As the surface area of the LSCF SAS catalyst is similar to the citric acid prepared sample, a similar catalytic activity was expected. However, this was not the case as the citric acid LSCF catalyst achieved a T₅₀ of 448 °C, while the catalysts prepared by SAS achieved had a T₅₀ of only 577 °C. The LSCF oxalic catalyst was found to be less active when compared to LSCF citric, as the T₅₀ increased from 448 to 475 °C (Fig. 5, Table 3). The surface area of the LSCF catalysts remained consistent across preparation methods, from 12 – 14 m² g⁻¹ (Table 3), indicating that for this set of catalysts the surface area does not determine the catalytic activity.

As suggested previously, the concentration of certain oxygen species present in the perovskite may play a large part in the activity. XPS can be used to determine the oxygen species present, with four main species: lattice oxygen from lanthanide elements, lattice oxygen from transition metals, surface hydroxyl species or molecular water [65, 88]. The LSCF catalysts prepared by the three different preparation methods all have these four oxygen species, with large peaks associated to lattice oxygen present in all catalysts (Fig. 6). By incorporating Fe into LSCF citric, the percentage of surface lattice oxygen species decreased slightly from 42% in LSC to 34% in LSCF citric, however, this is a large increase on the 1% seen in the SCF catalyst. This is possible even though all perovskites have an ABO₃ composition, all the catalysts have slightly different crystal structures. This depends on the ratio and size of the A and B site cations and the resulting A-O and B-O bond lengths. These catalysts have rhombohedral and cubic structures, of varying distortions. As a result, there are differing numbers of oxygen vacancies and lattice oxygen depending on the structural flexibility before collapse [89]. As the concentration of surface lattice oxygen and the surface area have remained constant in the LSC to LSCF catalysts, this indicates that another factor is contributing to the increase in activity for this catalyst. The lattice oxygen concentration decreased from 34% in the citric acid prepared catalyst to 29% in the SAS prepared catalyst, despite the comparable surface area. This resulted in a large decrease in activity, the T₅₀ increased from 448 (citric) to 577 °C (SAS), which could be due to a combination of the decrease in lattice oxygen and a reduction in purity between the two catalysts: the catalyst prepared using citric acid has a purity of 100% but the catalyst prepared by SAS has a purity of only 93%. LSCF oxalic has a lattice oxygen concentration of 34%, the same as the LSCF citric catalyst, however a decrease in N₂O conversion was noted, (T₅₀ increased from 448 to 475 °C) (Fig. 5). Although

Table 3 Comparison between all catalysts, preparation method, composition determined by MP-AES, surface area, phase purity and the temperature required for 50% conversion (T₅₀)

Catalyst	Preparation method	Pre-treatment temp (°C)	Calcination temp (°C)	Composition determined by MP-AES	Perovskite phase purity (%) ^a	Surface area (m ² g ⁻¹)	T ₅₀ (°C)	N ₂ O decomposition rate at 450 °C (mol h ⁻¹ kg ⁻¹)	Surface Lattice O (%) ^b
LSC	Citric acid	200	900	La _{0.8} Sr _{0.4} CoO _{3.9}	98	15	468	15.2	42
SCF	Citric acid	200	900	Sr _{1.5} CoFe _{0.2} O ₅	81	7	585	1.8	1
LSCF	Citric acid	200	550	LaSr _{0.5} CoFe _{0.1} O _{5.8}	100	13	448	22.8	34
LSCF	SAS	300	800	La _{0.8} Sr _{0.1} CoFe _{0.2} O _{5.2}	93	12	577	4.6	29
LSCF	Oxalic	300	750	La ₁ Sr _{0.3} CoFe _{0.2} O _{5.5}	100	14	475	17.2	34

^aPerovskite phase purity calculated using XRD diffraction pattern and the ratio between the single perovskite phase and any impurities.

^bLattice oxygen calculated by the ratio of lattice oxygen species to the sum of molecular water, transition metal lattice oxygen, hydroxyl species, as derived from XPS measurements.

Fig. 5 Effect of preparation method on LSCF catalysts for N_2O decomposition over the temperature range of 200 to 600 °C. Reaction conditions: 1% $\text{N}_2\text{O}/\text{He}$, total flow 100 mL min^{-1} . Filled square—LSCF Citric, filled triangle—LSCF SAS, filled circle—LSCF Oxalic. If error bars are not present, then smaller than symbol and less than 1%

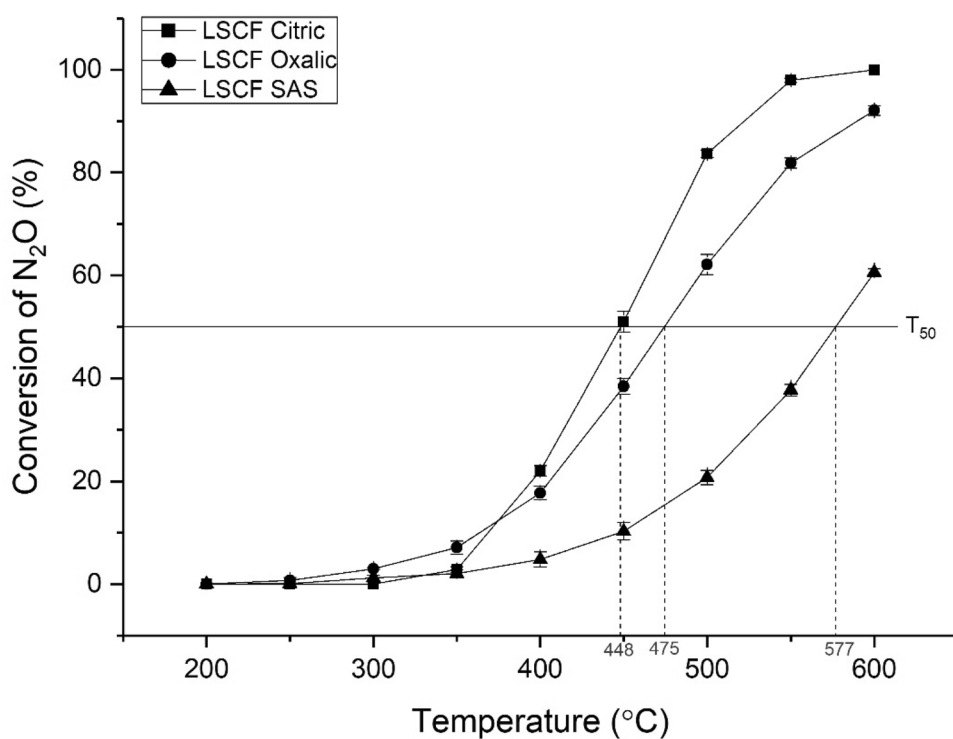
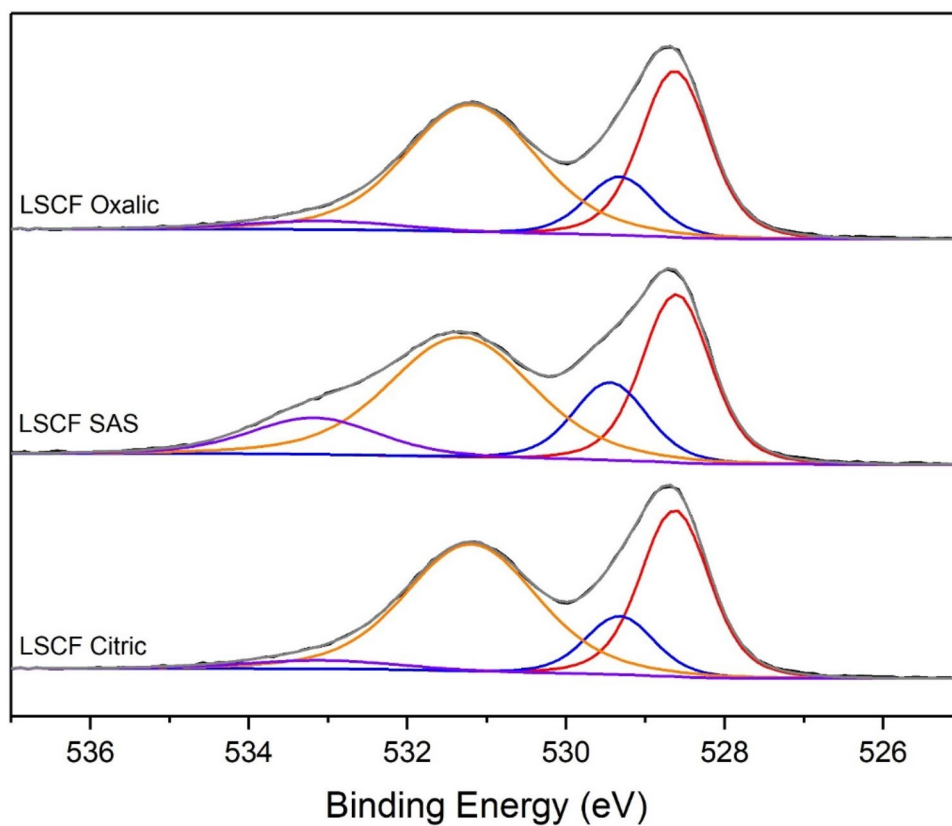


Fig. 6 XPS O 1s region of all LSCF catalysts. Fittings: Red—lattice O^{2-} , Blue—lattice O^{2-} transition metals, Orange—Carbonate CO_3^{2-} or hydroxyl species OH^- , and Purple—molecular water on surface

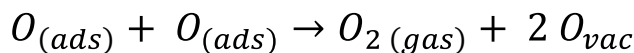
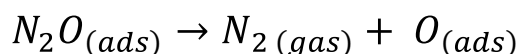


both catalysts have the same percentage of lattice oxygen, the mobility of the species present may be different. If all the oxygen present in the O 1s 531 eV peak is carbonate then the C 1s peak at 289 eV should be three times as large, due to the ratio of C and O in CO₃²⁻, therefore C 1s/ O 1s = 3, means only contribution from carbonate, if larger then contribution from carbonate and hydroxyl. The lanthanum 3d XPS spectra (Fig. S4) shows that all lanthanum containing catalysts have both lanthanum oxide and lanthanum carbonate present. As you can see from the data in Table S3, the SCF and LSCF SAS catalyst have only carbonate species present, but the LSC, LSCF Citric and LSCF Oxalic have both carbonate and hydroxyl species present at the surface. The catalysts that have only carbonate species present have poor catalytic activity, this could be due to a carbonate layer forming over the surface and blocking the active sites.

To expand the investigation into the oxygen species O₂-TPD was used to compare the mobility of the lattice oxygen species in the LSCF catalysts [28, 33]. Desorption below 300 °C indicates that chemically adsorbed O₂ is present. α-Oxygen desorbs at 300–550 °C, which is oxygen that is removed from the surface to form an oxygen vacancy [26, 76]. An oxygen vacancy is formed when oxygen is removed from the surface lattice structure, in the form of O₂ or H₂O, creating a defect site [90, 91]. Finally, above 550 °C, bulk lattice oxygen (β-O) desorbs [92, 93]. When comparing the O₂-TPD profiles of the three catalysts it is possible to compare the mobility of the lattice oxygen present. As there was no response in the region < 700 °C, only β-oxygen (also referred to as lattice oxygen) was present [26, 76]. A larger signal response during the O₂-TPD indicates a higher mobility of lattice oxygen present. The lower the temperature at which a response is measured, the more mobile the oxygen species present are [26, 76]. As mobility increases, the activity of the catalysts should also increase if the mobility of the oxygen is as important as previously described [93, 94]. In addition to lattice oxygen being required, oxygen mobility has also been shown to be crucial in the decomposition of N₂O due to the requirement to recombine O to form O₂ in the rate determining step. If there is a large amount of lattice oxygen present that is mobile, this can then react with atomic O from the dissociated N₂O, forming O₂ and regenerating the active site. Figure 7a displays the O₂-TPD profiles of LSCF prepared by the three preparation methods. As predicted by XPS, the SAS preparation produced the catalyst with the lowest response, with the onset of desorption at the highest temperature; this corresponds to lattice oxygen that is not mobile, hence producing a poorly active catalyst. The catalyst is not completely inactive, due to the small signal response seen at around 700 °C that corresponds to a small amount of mobile lattice oxygen. The oxalic and citric catalysts have similar responses at 750 °C, therefore, we consider that the mobility of the lattice oxygen is similar

at these temperatures and hence why at low temperatures the activity of the catalysts is similar. All catalysts show no response in the O₂-TPD between 300 and 700 °C, which is the region where α-Oxygen is present [26, 76]. α-Oxygen is also referred to as oxygen desorbed to form oxygen vacancies; this indicates that there are a very limited number of oxygen vacancies within this series of catalysts. Oxygen vacancies are important in this reaction as it is thought that the oxygen of N₂O could bind at a vacancy site and then initiate the decomposition of N₂O, as shown in Scheme 1.

If there are a limited number of the oxygen vacancies, then the catalyst may be limited in activity. The citric acid prepared catalyst produced a larger signal response than that of the oxalic catalyst above 750 °C and therefore has more mobile and available lattice oxygen for reaction. The properties of the catalysts are summarised in Table 3 with their activity for N₂O decomposition (T₅₀). The H₂-TPR shows the reducibility of the perovskites and therefore gives an indication about the mobility of the oxygen species due to the strength of the Co–O bond [74]. As mentioned previously; the reduction of surface-adsorbed O species or non-stoichiometric excess oxygen reduction of oxygen species, including oxygen adsorbed on the oxygen deficiency, take place between 200 and 300 °C [75, 76] Followed by the step wise reduction of Co³⁺ to Co²⁺ between 200 and 360 °C and Co²⁺ to Co⁰ between 450 and 540 °C [77, 78]. As Fe is the only other reducible metal in these catalysts, Fe³⁺ to Fe^{3+/2+} reduction takes place at around 300 °C, followed by the reduction of Fe^{3+/2+} to Fe⁰ at around 700 °C [81]. The H₂-TPR of LSCF prepared by the three preparation methods are given in Fig. 7b. LSCF SAS and oxalic show very similar H₂-TPR profiles, comprised of Co³⁺ to Co²⁺ and Fe³⁺ to Fe^{3+/2+} reductions which occur between 250 and 450 °C, followed by the simultaneous reduction of Co²⁺ to Co⁰ and Fe^{3+/2+} to Fe⁰ between 550 and 800 °C. The H₂-TPR profile of LSCF citric is slightly different, the reduction of Co³⁺



Scheme 1 N₂O decomposition mechanism on the surface of a perovskite. Showing the use of oxygen vacancies (O_{vac}) and the importance of the mobility of lattice oxygen (O_{ads})

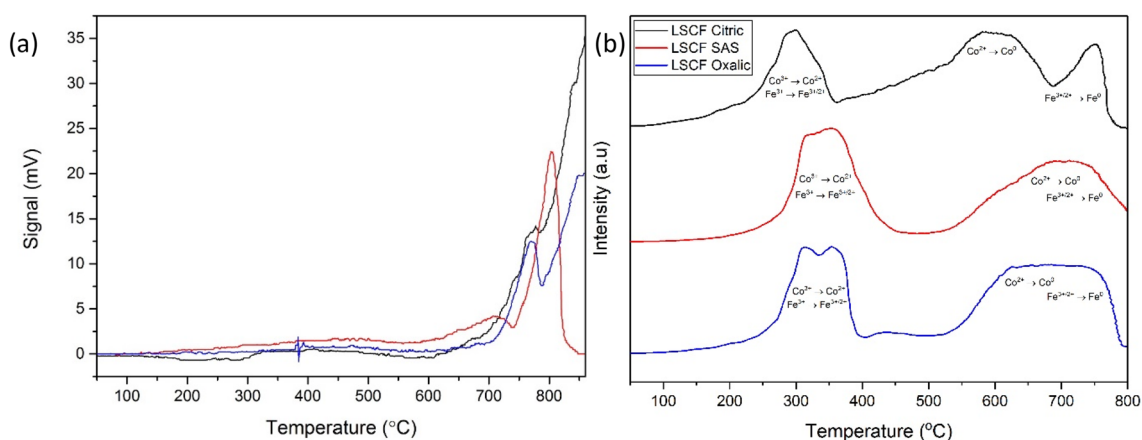


Fig. 7 **a** Oxygen temperature programmed desorption (O_2 -TPD) of LSCF catalysts, Black—Citric prep, Red—SAS prep, Blue—Oxalic prep. **b** H_2 -TPR of all LSCF catalysts, performed at $5\text{ }^\circ\text{C min}^{-1}$ up to $800\text{ }^\circ\text{C}$, under a flow of 10% H_2/Ar .

to Co^{2+} and Fe^{3+} to $\text{Fe}^{3+/2+}$ occurs at a slightly lower temperature between 200 and $350\text{ }^\circ\text{C}$, followed by the reduction of Co^{2+} to Co^0 between 500 and $700\text{ }^\circ\text{C}$, with the final step assigned to the reduction of $\text{Fe}^{3+/2+}$ to Fe^0 between 690 and $780\text{ }^\circ\text{C}$. The decreases in the reduction temperature of the Co species in LSCF Citric indicates that the Co–O bond strength is weaker and the mobility of the oxygen species is increased, which is vital for N_2O decomposition, as the recombination of surface oxygen is commonly the rate determining step [34, 35]. The combination of H_2 -TPR and O_2 -TPD indicate why the LSCF citric catalyst is the most active for N_2O decomposition, due to the presence of a weaker Co–O bond, and an increased oxygen mobility, aiding the recombination of oxygen species enabling the regeneration of active sites on the surface of the catalyst.

The Co $2p$ XPS spectra is shown in Fig. S8, all catalysts have a peak present at 779.2 eV due to the presence of Co_3O_4 , this is a mixed oxidation state of Co(II) and Co(III) [63]. The presence of Co(II) species leads to the formation of a satellite at *ca.* 789 eV [63]. The broader the line shape the greater the Co $^{2+/3+}$ ratio, therefore the catalyst with the lowest $\text{Co}^{2+/3+}$ is LSC, followed by LSCF Oxalic and LSCF SAS [95, 96]. This indicates that these catalysts have very little redox capabilities. This is confirmed by H_2 -TPR which shows a high reduction temperature required for the reduction of Co, indicating a strong Co–O bond, this subsequently limits the activity of the catalysts. Both the LSC and LSCF Citric have a much broader line shape than the other catalysts and these are the two most active catalysts. The improved catalytic activity can be attributed to the improved redox capabilities as shown by XPS and, in the case of LSCF citric, H_2 -TPR.

The most active LSCF catalyst was tested at $450\text{ }^\circ\text{C}$ for 24 h to give an indication of the stability of the catalysts under reaction conditions (Fig. S9). The LSCF citric catalyst

has a slight induction period of *ca.* 1.5 h , but the catalyst did not lose any activity over the time-period tested.

LSCF citric catalyst has a T_{50} of $448\text{ }^\circ\text{C}$ and a decomposition rate of $22.8\text{ mol h}^{-1}\text{ kg}^{-1}$, this compares to Kumar et al. with a T_{50} of $442\text{ }^\circ\text{C}$ and a decomposition rate of $1.2\text{ mol h}^{-1}\text{ kg}^{-1}$ using a $\text{Pr}_{0.2}\text{Ba}_{0.8}\text{MnO}_3$ catalyst [29], and Hutchings and co-workers who prepared a $\text{Pr}_{0.75}\text{Ba}_{0.25}\text{CoO}_3$ catalyst that has a T_{50} of $410\text{ }^\circ\text{C}$ and a decomposition rate of $32\text{ mol h}^{-1}\text{ kg}^{-1}$ [33], therefore the LSCF is amongst the most active in literature.

5 Conclusions

We have shown that by altering the ratios of the A and B site cations it is possible to produce a pure phase perovskite at low temperatures, and by varying the preparation method it is possible to produce perovskites with different ratios of oxygen species. This work confirms the importance of lattice oxygen species that have high oxygen mobility for the decomposition of N_2O . Mobile lattice oxygen has been shown to be crucial, as the rate-limiting step in the decomposition of N_2O is the formation of molecular oxygen. This is limited by adsorbed O species being close enough for recombination. However, if there are mobile lattice oxygen species present then these can aid recombination and regenerate the active site for N_2O decomposition. In the case of LSCF the activity correlates with the weaker Co–O bond and more mobile lattice oxygen present. The most mobile lattice oxygen, and therefore highest activity, was obtained with the citric acid preparation. LSCF citric catalyst has a T_{50} of $448\text{ }^\circ\text{C}$ and a decomposition rate of $22.8\text{ mol h}^{-1}\text{ kg}^{-1}$ compared to other perovskites used in literature for N_2O decomposition this is amongst the most active.

Supplementary Information The online version contains supplementary material available at <https://doi.org/10.1007/s10562-021-03619-3>.

Acknowledgements We thank the ERC for funding 'After the GoldRush' code, ERC-AtG-291319

Compliance with ethical standards

Conflict of interests The authors declare they have no conflict of interests.

Open Access This article is licensed under a Creative Commons Attribution 4.0 International License, which permits use, sharing, adaptation, distribution and reproduction in any medium or format, as long as you give appropriate credit to the original author(s) and the source, provide a link to the Creative Commons licence, and indicate if changes were made. The images or other third party material in this article are included in the article's Creative Commons licence, unless indicated otherwise in a credit line to the material. If material is not included in the article's Creative Commons licence and your intended use is not permitted by statutory regulation or exceeds the permitted use, you will need to obtain permission directly from the copyright holder. To view a copy of this licence, visit <http://creativecommons.org/licenses/by/4.0/>.

References

- Elkins J, Dlugokencky E, Hall B, et al (2020). <https://www.n2olevels.org/>. Accessed 27 May 2020
- Pérez-Ramírez J, Kapteijn F, Schöffel K, Moulijn JA (2003) Appl Catal B Environ 44:117–151
- Weimann J (2003) Best Pract Res Clin Anaesthesiol 17:47–61
- Forster P, Ramaswamy V (2007) In: Climate Change 2007: The Physical Science Basis. Contribution of Working Group I to the Fourth Assessment Report of the Intergovernmental Panel on Climate Change, pp 131–234
- Intergovernmental Panel on Climate Change (2008) Climate change 2007: synthesis report. Intergovernmental Panel on Climate Change
- Intergovernmental Panel on Climate Change (2013) Climate Change 2013: the physical science basis. Contribution of Working Group I to the Fifth Assessment Report of the Intergovernmental Panel on Climate Change
- Maroufi SS, Gharavi MJ, Behnam M, Samadikuchaksaraei A (2011) Iran J Public Health 40:75–79
- Kapteijn F, Rodriguez-Mirasol J, Moulijn JA (1996) Appl Catal B Environ 9:25–64
- Zabilskiy M, Erjavec B, Djinović P, Pintar A (2014) Chem Eng J 254:153–162
- Zhou H, Hu P, Huang Z et al (2013) Ind Eng Chem Res 52:4504–4509
- Abu-Zied BM, Soliman SA, Abdellah SE (2015) J Ind Eng Chem 21:814–821
- Stelmachowski P, Maniak G, Kaczmarczyk J et al (2014) Appl Catal B Environ 146:105–111
- Parres-Esclapez S, Illan-Gomez MJ, de Lecea CSM, Bueno-Lopez A (2010) Appl Catal B Environ 96:370–378
- Kapteijn F, Mul G, Marbán G, et al (1996). In: 11th International Congress on Catalysis: 40th Anniversary, vol 101, pp 641–650
- Labhasetwar N, Saravanan G, Kumar Megarajan S et al (2015) Sci Technol Adv Mater 16:036002
- Konsolakis MI (2015) ACS Catal 5:6397–6421
- Hwang J, Rao RR, Giordano L et al (2017) Science 358:751–756
- Isupova LA, Alikina GM, Tsybulya SV et al (2001) Int J Inorg Mater 3:559–562
- Huang C, Wang X, Shi Q et al (2015) Inorg Chem 54:4002–4010
- Afzal S, Quan X, Zhang J (2017) Appl Catal B Environ 206:692–703
- Meng L, Sun C, Wang R et al (2018) J Am Chem Soc 140:17255–17262
- Zhang M, Dai S, Chandrabose S et al (2018) J Am Chem Soc 140:14938–14944
- Ke W, Spanopoulos I, Tu Q et al (2019) J Am Chem Soc 141:8627–8637
- Tanaka H, Misono M (2001) Curr Opin Solid State Mater Sci 5:381–387
- Marchetti L, Forni L (1998) Appl Catal B Environ 15:179–187
- Zhu J, Li H, Zhong L et al (2014) ACS Catal 4:2917–2940
- Russo N, Mescia D, Fino D et al (2007) Ind Eng Chem Res 46:4226–4231
- Ivanov DV, Pinaeva LG, Isupova LA et al (2013) Appl Catal A Gen 457:42–51
- Kumar S, Vinu A, Subrt J et al (2012) Catal Today 198:125–132
- Ivanov DV, Sadvovskaya EM, Pinaeva LG, Isupova LA (2009) J Catal 267:5–13
- Ivanov DV, Pinaeva LG, Isupova LA et al (2011) Catal Lett. 141:322–331
- Ishihara T, Ando M, Sada K et al (2003) J Catal 220:104–114
- Richards N, Carter JH, Parker LA et al (2020) ACS Catal 10:5430–5442
- Guesmi H, Berthomieu D, Kiwi-Minsker L (2008) J Phys Chem C 112:20319–20328
- Sang C, Kim BH, Lund CRF (2005) J Phys Chem B 109:2295–2301
- Hansen N, Heyden A, Bell AT, Keil FJ (2007) J Phys Chem C 111:2092–2101
- Bulushev DA, Kiwi-minsker L, Renken A (2004) Ind Eng Chem Res 211:2004
- Sun K, Xia H, Hensen E et al (2006) J Catal 238:186–195
- Pirngruber GD (2003) J Catal 219:456–463
- Wood B, Reimer JA, Bell AT (2002) J Catal 209:151–158
- Pirngruber GD, Roy PK, Prins R (2007) J Catal 246:147–157
- Richards N, Nowicka E, Carter JH et al (2018) Top Catal 61:1983–1992
- Peña MA, Fierro JLG (2001) Chem Rev 101:1981–2017
- Ishikawa S, Jones DR, Iqbal S et al (2017) Green Chem 19:225–236
- Evans CD, Kondrat SA, Smith PJ et al (2016) Faraday Discuss 188:427–450
- Hutchings GJ, Bartley JK, Lopez-Sanchez JA et al (2001) J Catal 197:232–235
- Marin RP, Kondrat SA, Pinnell RK et al (2013) Appl Catal B Environ 140–141:671–679
- Miedziak PJ, Tang Z, Davies TE et al (2009) Appl Catal B Environ 19:8619–8627
- Trikalitis PN, Pomonis PJ (1995) Appl Catal A Gen 131:309–322
- Buassi-Monroy OS, Luhrs CC, Chávez-Chávez A, Michel CR (2004) Mater Lett 58:716–718
- Majid A, Tunney J, Argue S et al (2005) J Alloys Compd 398:48–54
- Robert R, Logvinovich D, Aguirre MH et al (2010) Acta Mater 58:680–691
- Deganello F, Marci G, Deganello G (2009) J Eur Ceram Soc 29:439–450
- Sihaib Z, Puleo F, Pantaleo G et al (2019) Catalysts 9:1–18
- Xia Z, Sun J, Du H et al (2010) J Mater Sci 45:1553–1559
- Thermofisher (2019) <https://xpssimplified.com/elements/praseodymium.php>. Accessed 19 Mar 2019

57. Thermofisher (2019) <https://xpssimplified.com/elements/barium.php>. Accessed 19 Mar 2019
58. Thermofisher (2019) <https://xpssimplified.com/elements/strontium.php>. Accessed 19 Mar 2019
59. Thermofisher (2019) <https://xpssimplified.com/elements/lanthanum.php>. Accessed 19 Mar 2019
60. Fierro JLG, Tejuca LG (1987) *Appl Surf Sci* 27:453–457
61. Tabata K, Hirano Y, Suzuki E (1998) *Appl Catal A Gen* 170:245–254
62. Thermofisher (2019) <https://xpssimplified.com/elements/iron.php>. Accessed 19 Mar 2019
63. Thermofisher (2019) <https://xpssimplified.com/elements/cobalt.php>. Accessed 19 Mar 2019
64. Morris MA, Connell MO, Norman AK, Hu CF (1999) *Catal Today* 47:123–132
65. Worayingyong A, Kangvansura P, Kityakarn S (2008) *Colloids Surf A Physicochem Eng Asp* 320:123–129
66. Zhang-Steenwinkel Y, Beckers J, Blik A (2002) *Appl Catal A Gen* 235:79–92
67. Kumar S, Teraoka Y, Joshi AG et al (2011) *J Mol Catal A Chem* 348:42–54
68. Wang P, Yao L, Wang M, Wu W (2000) *J Alloys Compd* 311:53–56
69. Stoch J (1991) *J Alloys Compd* 17:165–167
70. Niania M, Podor R, Britton TB et al (2018) *J Mater Chem A* 6:14120–14135
71. Thermofisher (2020) <https://xpssimplified.com/elements/carbon.php>. Accessed 23 Jun 2020
72. Tanigawa S, Takashima T, Irie H (2017) *J Mater Sci Chem Eng* 05:129–141
73. Dupin JC, Gonbeau D, Vinatier P, Levasseur A (2000) *Phys Chem Chem Phys* 2:1319–1324
74. Sadykov VA, Bulgakov NN, Muzykantov VS et al (2004) *Mixed ionic electronic conducting perovskites for advanced energy systems*. Springer, Dordrecht, pp 53–74
75. Gu Q, Wang L, Wang Y, Li X (2019) *J Phys Chem Solids* 133:52–58
76. Zhu J, Zhao Z, Xiao D et al (2005) *J Mol Catal A Chem* 238:35–40
77. Osazuwa OU, Cheng CK (2017) *J Clean Prod* 148:202–211
78. Fierro JLG, Peña MA, González Tejuca L (1988) *J Mater Sci* 23:1018–1023
79. Erdenee N, Enkhnarant U, Galsan S, Pagvajav A (2017) *J Nanomater* 2017:1–8
80. Kuznetsova T, Sadykov V, Batuev L et al (2005) *React Kinet Catal Lett* 86:249–256
81. Pour AN, Taghipoor S, Shekarriz M et al (2009) *J Nanosci Nanotechnol* 9:4425–4429
82. Voorhoeve RJH, Johnson DW, Remeika JP, Gallagher PK (1977) *Science* 195:827–833
83. Centi G, Perathoner S (2008) *Microporous Mesoporous Mater* 107:3–15
84. Alini S, Basile F, Blasioli S et al (2007) *Appl Catal B Environ* 70:323–329
85. Dacquin JP, Dujardin C, Granger P (2008) *Catal Today* 137:390–396
86. Yuan J, Li SS, Yu L et al (2013) *Energy Environ Sci* 6:3308–3313
87. Wang L-C, Liu Q, Chen M et al (2007) *J Phys Chem C* 111:16549–16557
88. Merino NA, Barbero BP, Eloy P, Cadús LE (2006) *Appl Surf Sci* 253:1489–1493
89. Ji Q, Bi L, Zhang J et al (2020) *Energy Environ Sci* 13:1408–1428
90. Puigdollers AR, Schlexer P, Tosoni S, Pacchioni G (2017) *ACS Catal* 7:6493–6513
91. Liu L, Zhou F, Wang L et al (2010) *J Catal* 274:1–10
92. Pan KL, Yu SJ, Yan SY, Chang MB (2014) *J Air Waste Manag Assoc* 64:1260–1269
93. Dacquin JP, Lancelot C, Dujardin C et al (2009) *Appl Catal B Environ* 91:596–604
94. Li C, Shen Y, Zhu S, Shen S (2014) *RSC Adv* 4:29107–29119
95. Dudric R, Vladescu A, Rednic V et al (2014) *J Mol Struct* 1073:66–70
96. Giraudon JM, Elhachimi A, Leclercq G (2008) *Appl Catal B Environ* 84:251–261

Publisher's Note Springer Nature remains neutral with regard to jurisdictional claims in published maps and institutional affiliations.

Authors and Affiliations

Nia Richards¹ · Luke A. Parker^{1,2} · James H. Carter¹ · Samuel Pattison¹ · David J. Morgan¹ · Nicholas F. Dummer¹ · Stanislaw E. Golunski¹ · Graham J. Hutchings¹

¹ Cardiff Catalysis Institute, School of Chemistry, Cardiff University, Cardiff CF10 3AT, UK

² Inorganic Chemistry and Catalysis Debye Institute for Nanomaterials Science, Utrecht University, Universiteitsweg 99, 3584CG Utrecht, The Netherlands